Catalysis Science & Technology

Accepted Manuscript

ROYAL SOCIETY OF CHEMISTRY

www.rsc.org/catalysis

Catalysts, Kinetics and Process Optimization for the Synthesis of Methyl Acrylate over Cs-P/γ-Al_2O_3

Guoliang Zhang,[a] Honghua Zhang,[b] Dan Yang,[b] Chunshan Li,[b] Zhijian Peng,[*a] and Suojiang Zhang[*b]

Bifunctional catalysts Cs-P/γ-Al_2O_3 were developed and firstly applied in one-step synthesis methyl acrylate (MA) using methyl acetate (Ma) and formaldehyde (FA). The catalysts were prepared with impregnation and characterized by XRD, TEM, TG/DTA, N_2 adsorption–desorption, NH_3 and CO_2-TPD methods. The catalytic performance was evaluated using a fixed-bed microreactor. Experimental results indicated the P-loading had significantly influence on catalytic activity by modifying the acid-base surface properties of the catalyst. The process optimization using response surface methodology (RSM) was performed and the interactions operational variables including Ma/FA molar ratio, reaction time and temperature were elucidated. And then the kinetic of the aldol condensation reaction was studied through pseudo-homogeneous kinetic model. Besides, the lifetime of optimum Cs10%-P5%/γ-Al_2O_3 catalyst was evaluated continuing 400 h, and did not exhibit obviously deactivation.

1. Introduction

Acrylic acid (AA) and esters are the most versatile series of monomers that provide characteristic performance to thousands of polymer formulations owing to their α, β-unsaturated carboxyl structure.[1] AA is primarily used as feedstock to produce water-soluble acrylate coatings in the paint industry, and superabsorbent polymers (SAP) in the diaper industry, as well as in the production of detergents, dispersants, flocculants, adhesives, fibers and paints. To date, nearly all commercial AA are produced via the two-stage oxidations of propylene with air. However, the propylene is the most expensive component feedstock for AA production which is greatly influenced by crude oil price. Due to oil shortage, the high price of propylene makes this route uncompetitive. Therefore, development of alternative routes for AA production is necessary. In recent decades, one-step synthesis of acrylic acid and ester via aldol condensation of acetic acid or Ma with FA has been studied and developed.

The key to realize this technique is the acquirement of high efficient catalyst. According to the previous work in the past few years, both of the acid and base catalysts are catalytically active for aldol condensation reaction. The commonly used acid catalysts are V_2O_5, P_2O_5, Nb_2O_5, WO_3, ZrO_2 and Ta_2O_5.[2-7] And the base catalysts often used are Na, K, Cs, Sr and Mg oxide or hydroxide on appropriate supports.[8-17] Bailey et al.[8] studied the activity of alkali metal cations on SiO_2 and found that catalyst activity and selectivity depended on alkali metal cation, which increased in the Li < Na < K < Cs. Solid divanadium dioxides pyrophosphate demonstrates the higher catalyst performance among the aforementioned acid catalysts and is later improved to form V-Si-P by combining $V_2O_2(P_2O_7)$ with silica gel.[18-19] M. Ai[20] prepared silica-supported tin phosphate with 1:8:2.3 Sn/Si/P atomic ratio and obtained a similar catalyst activity as that of as silica-supported vanadium phosphate with 1:8:2.2 V/Si/P atomic ratio. Yoo[10] studied the effect of the doped metals on silica-supported Cs catalyst and found that Bi-doped system showed the best catalyst performance compared with other catalysts doped with Pb, Ti and La. Recently acid-base bifunctional catalyst became a research hotspot.[21-26] Yan et al.[27] used an SBA-15 mesoporous molecular support impregnated with cesium oxide to catalyze the reaction. Li et al.[21] reported that the Zr–Mg–Cs/SiO_2 bifunctional catalyst exhibited higher activity than that of SBA-15 supported metal-doped Cs ion catalysts.[22] Tai et al.[23] prepared various catalysts consisting of MgO, SiO_2, Al_2O_3 and ZrO_2 with and without added Cs and suggested that both strong solid acid and base sites were ineffective on catalyzing the aldol condensation reaction, and the moderate acidity corresponded to higher selectivity.

Catalyst design is a complex engineering problem involving multiple impacts to consider. However, RSM is an efficient statistical technique for building models, optimization of multifactor experiments, and evaluation of effects of numerous factors for the required responses which was adopted to optimize the process of the esterification of oleic acid due to RSM can produce huge information by performing a small number of experiments and also provides the possibility of observing the effects of single variables and their combinations of interactions on the response.[28-31] In the present work, the optimization of process parameters of the reaction conditions for the synthesis of methyl acrylate is analyzed by RSM. Besides, the pseudo-homogeneous (P-H) model, which have been used to various

[a] School of Engineering and Technology
China University of Geosciences, Beijing 100083 (P.R. China)
E-mail addresses: pengzhijian@cugb.edu.cn (Z. Peng)
[b] Beijing Key Laboratory of Ionic Liquids Clean Process
Institute of Process Engineering，Chinese Academy of Sciences
Beijing 100190 (P.R. China)
E-mail addresses: csli@home.ipe.ac.cn (C. Li).
E-mail addresses: sjzhang@home.ipe.ac.cn (S. Zhang).

esterification reactions for kinetic investigation, is also introduced to this work. The combination of RSM and P-H model for aldol condensation reaction of the Ma with FA over solid catalyst has not reported so far.

In this work, Cs-P/γ-Al_2O_3 catalysts were prepared by impregnation. Phosphate was added to regulate the acidity and basicity of the catalyst due to phosphorus is reported to modify and balance the acid–base surface properties of the catalyst and also to use as a support stabilizer.[32-37] The catalytic performances of the catalysts were carried out in a fixed-bed tubular microreactor. Three important variables of Ma/FA molar ratio, reaction time and reaction temperature were optimized by RSM. And the kinetic equation is obtained with the pseudo-homogeneous model incorporating the effects of reaction temperature.

2. Experimental section

2.1 Catalyst Preparation

Methyl acetate (≥99.0%), methanol (≥99.0%), trioxymethylene (≥98%), cesium carbonate (≥98.0%), and diammonium hydrogen phosphate (≥99.0%) are of analytical grade bought from Sinopharm Chemical Reagent Company. The γ-Al_2O_3 spheres were obtained from commercial company. The γ-Al_2O_3 supports were initially ground, sieved to obtain 20 to 40 mesh-size portions. All the supports dried at 550°C for 4 h before impregnation.

The Cs/γ-Al_2O_3 catalysts were prepared by wet impregnation of the support with an aqueous solution with appropriate Cs concentration (Cs content based on Cs_2O weight percent of the support). The mixtures incubated at room temperate for 12 h and then dried in an oven at 120°C for 6 h. And then the resulting solids were calcined at 550°C for 6 h under flowing air. Cs-P/γ-Al_2O_3 catalysts were prepared as the same way except that two aqueous solution of Cs_2CO_3 and $(NH_4)_2HPO_4$ were mixed before impregnation. The Cs10%-P5%/γ-Al_2O_3 catalyst were prepared as follows: the γ-Al_2O_3 supports (30 g) were impregnated with 30ml aqueous solution containing the desired amount of cesium carbonate (Cs_2CO_3 3.674 g, 1.27 mmol) and the diammounium hydrogen phosphate [$(NH_4)_2HPO_4$ 2.977 g, 2.54 mmol]. The other catalysts were prepared in the same way.

2.2 Catalyst Characterization

X-ray diffraction (XRD) patterns were obtained using X-Pert PRO MPD diffractometer (PANalytical B.V., the Netherlands) operated at 40 kV and 40 mA with Cu-Kα radiation. The angle (2θ) was measured in 20°/min step between 2θ = 5 and 90°. Transmission electron microscopy (TEM) images were obtained using a JEM-2100 electron microscope (JEOL, Japan) operated at 200 kV. For the TEM measurements, the powdered samples were dispersed in ethanol to form slurry, which was deposited on a copper microgrid and covered with a carbon film. Sample weight loss and the temperature associated with phase transformation were determined by thermogravimetry and differential thermal analysis (TG/DTA) using a DTG-60H analyzer (Shimadzu, Japan). The samples were heated from room temperature to 800°C at 10 °C /min in 30 mL/min air flow. BET specific surface area were derived from N_2 adsorption-desorption isotherms under liquid N_2 temperature using Micromeritics ASAP 2020 Plus (Micromeritics, USA), the samples were degassed at 350°C for 12 h. Acid-base properties were determined using Autochem II 2920 from Micrometrics. For acidity measurements, about 50 mg of the samples were placed in quartz tubes and pretreated under helium flow at 450°C for 1 h. Subsequently, 10 vol. % NH_3 in helium was passed through the samples at 50°C for 30 min. The samples were then purged with pure helium at 50°C for 1 h. When the baseline was stable, the NH_3 desorption rate was monitored in helium flow up to 700°C at 10°C/min heating rate using a thermal conductivity detector. The basicity of the catalysts was measured similar to that of the acidity measurements. XPS spectra were obtained on a Thermo Scientific Escalab 250Xi X-ray photoelectron spectrometer equipped with a conventional hemispherical analyzer. The latter was operated at constant pass energy of 100 eV in the fixed transmission mode. The incident radiation used was a monochromatic Al Kα (1486.6 eV) operated at 420 W (14 kV; 30 mA). Analysis was performed using a takeoff angle of 90°, and the base pressure in the analysis chamber was ~10^{-9} mbar. The analyzed surface area was ~3 mm^2. The survey and multiregions spectra were recorded for C1s, Cs3d and P2p photoelectron peaks.

2.3 Measurement of Catalyst Performance

A continuous-flow fixed-bed tubular microreactor was filled with 5 g of catalyst for catalyst performance characterizations. The reactor was made of a stainless steel tube, 70 cm L x 1.8 cm ID, mounted vertically in triple-zone furnace. The catalyst (5 g) was held in the second zone by glass wool and quartz sands packed in the first and third zone. The mixed reactant consisted of 5:1:0.75 Ma/FA/CH_3OH molar ratios, was fed to the reactor using a metering pump. FA was fed as trioxane, which was dissolved in Ma. The formation of acetic acid due to the hydrolysis of Ma causes pipeline corrosion and reacts with FA to form acrylic acid. The addition of methanol can inhibit the hydrolysis of Ma.

The products were analyzed by Shimadzu GC 2010 plus with BID detector. The isobutanol was added to the product as an internal standard. The activity of the catalyst was measured by testing the yield of MA (mol), the selectivity of MA (mol) and conversion of FA (mol). The experimental data were analyzed as follows:

$$\text{Seletivity of MA} = \frac{MA_{out,mol}}{FA_{in,mol} - FA_{out,mol}} \text{x } 100\%$$

$$\text{Conversion of MA} = \frac{FA_{in,mol} - FA_{out,mol}}{FA_{in,mol}} \text{ x } 100\%$$

$$\text{Yield of MA} = \text{Selctivity of MA x Conversion of FA}$$

2.4 Response surface methodology

In this study, an experimental design for the series of parameters used for MA production through aldol condensation of Ma with FA over Cs10%-P5%/γ-Al_2O_3 was built by RSM with the Design-Expert Version 8.0.7.1 (Stat-Ease, Inc., Minneapolis, USA).[38] Box–Behnken experimental design was chosen to predict the relationship between the yield and Ma/FA molar ratio (X_1), reaction temperature (X_2), reaction time (X_3 = 1/liquid hourly space velocity). According to a 3^3 Box−Behnken experimental design, a total of 17 experiments were built, which included 12 factorial points and 5 centering points. The aforementioned three experimental variables were tested at three levels coded with either a minus sign (-1, lower value), zero (0, central value), or a plus sign (+1, higher value). The coded values of these factors were obtained by the equation:

$$X_i = \frac{X_i - X_0}{\Delta X_i} \quad (1)$$

where X_i, x_i, and x_0 (i = 1 – 3) represented the coded, real, and central value of the independent variable, respectively, and Δx_i was (variable at high level − variable at low level)/2 (see Table 1).

Table 1. Parameter levels and coded values used in the Box-Behnken Design.

variables	symbol	Coded levels		
		-1	0	1
Molar ratio (Ma/FA)	X_1	3	5	7
Temperature (°C)	X_2	340	360	380
Reaction time (min)	X_3	15	30	45

A model equation based on second-degree polynomial suggested by RSM was used to predict the optimum value and analyze the interaction between response of experimental design (the yield of MA) and the variables (X_1, X_2, X_3). The quadratic equation model was expressed as:

$$Y = \beta_0 + \sum_{i=1}^{k} \beta_i X_i + \sum_{i=1}^{k} \beta_{ii} X_{ii}^2 + \sum_{i=1}^{k} \beta_{ij} X_i X_{ij} + e \quad (2)$$

where Y was the predicted response (the yield of MA); β_0, β_i, β_{ii}, and β_{ij} were the regression coefficients representing, the linear terms, the squared terms for the variable i, and the interaction terms between variables i and j, respectively; X_i, X_{ii}, and X_{ij} represented interactive, quadratic, and the linear terms of the coded independent variables, respectively; k was the total number of designed variables; e represented the random error. The fitted polynomial equation visualized the relationship between the response and experimental variables at various coded levels and deduced the optimum conditions by response surface and contour plots. The coefficient of determination (R^2) was used to evaluate the accuracy and general ability of the second-order multiple regression model. Its regression coefficient significance was tested by F-test value.

2.5 Kinetic studies

The aldol condensation reaction of FA (A) with Ma (B) for producing MA (C) and water (D) over Cs10%-P5%/ γ-Al_2O_3 catalyst can be given as:

$$CH_2O\ (A) + CH_3COOCH_3\ (B) \rightarrow CH_2{=}CHCOOCH_3\ (C) + H_2O\ (D)$$

The kinetic model was built on the following assumptions: a) there was no concentration gradient and temperature gradient between the solid catalyst and gas phase in the fixed bed; b) the rate of the noncatalyzed reactions was negligible compared with the catalyzed reactions; c) the activity of the catalytic sites on the surface of the catalyst was assumed to be same; d) the internal and external mass transfer limitations of the heterogeneous catalyst had been excluded by studying the effect of flow velocity and catalyst particle size. Thus, the reaction rate equation could be defined as:

$$r = -\frac{dC_A}{dt} = k_1 C_A^a C_B^b - k_2 C_C^c C_D^d \quad (3)$$

where C_A, C_B, C_C and C_D presented the concentrations of FA, Ma, MA and water, respectively; k_1 and k_2 were the forward and reverse rate constants, respectively; a, b, c and d were the reaction order of FA, Ma, MA and water, respectively.

In order to make simple calculation, the reaction could be considered as irreversible reaction as there was no FA and Ma can be found when MA and water as reactants were passing through the fix bed under the same condition. Besides, the molar ratio of the Ma to FA was 5/1, so the changes of the kC_B^b can be considered negligible. Therefore, the Eq. 3 can be converted to Eq. 4 and 5:

$$r = -\frac{dC_A}{dt} = kC_A^a \quad (4)$$

$$\ln r = \ln k + a \ln C_A \quad (5)$$

The plots of lnr can be used as a function of $\ln C_A$. The values of C_A can be obtained by Shimadzu GC 2010 plus with BID. The relationship between C_{FA} and reaction time t was performed nonlinear fitting through Exponential Decay 1 (ExpDec1) Function from Origin 8 as the Eq. 6. Therefore, the reaction rate r can be obtained using differential method. The plot of lnr vs $\ln C_A$ was analyzed by linear regression. Both reaction order a and lnk can be obtained from the slope and intercept from the linear regression analysis.

$$y = A_1 * \exp(-\frac{x}{t_1}) + y_0 \quad (6)$$

The reaction rate k was a function related to reaction temperature, and their correlation was described by the Arrhenius equation:

$$k = Ae^{-\frac{E_a}{RT}} \quad (7)$$

The Eq. 7 can be also converted to Eq. 8

$$\ln k = \left(-\frac{E_a}{R}\right) * \frac{1}{T} + \ln A \quad (8)$$

Therefore, the plot of lnk vs 1/T was represented by a straight line. Both the frequency factor A and the activation energy Ea were obtained by linear regression.

3. Results and discussion

3.1 catalyst characterization

The XRD patterns of Cs/γ-Al_2O_3 with different Cs-loadings are shown in the Figure 1. Except the γ-Al_2O_3 phase peaks, no characteristic diffraction peaks of Cs species are observed because of its lower loading content and weak crystallization, on the other hand, also implying the good dispersion of the very small Cs species cluster on the γ-Al_2O_3 surface at initial loadings. When the Cs-loading is up to 15%, the Cs_2CO_3 phase peaks can be seen and the intensity of these signal increased at higher Cs-loading. Besides, the cesium superoxide (CsO_2) is also observed at high Cs-loading which has no activity for the reaction.[23] However, when P is introduced, from the XRD patterns of the Cs-P/γ-Al_2O_3 catalysts (Figure 2), only the diffraction peaks of γ-Al_2O_3 phase can be detected even at high P-loading suggesting that the phosphate species exist as amorphous phase with high dispersion on the surface of γ-Al_2O_3.

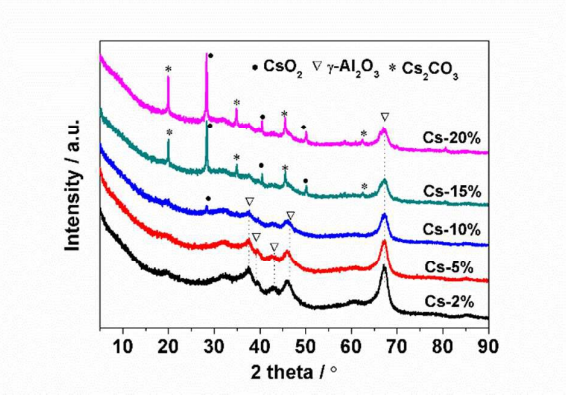

Figure 1. the XRD pattern of the Cs/γ-Al_2O_3 with different Cs-loadings.

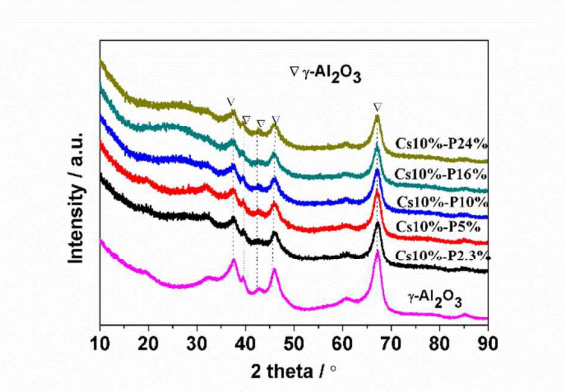

Figure 2. XRD patterns of Cs-P/γ-Al_2O_3 catalysts with different P-loadings.

In order to know its physical and chemical changes during calcination process, the TG and DTA curves of Cs-P/γ-Al_2O_3 samples before calcination are obtained and shown in Figure 3. Two distinguishing endothermic peaks at 89 and 180°C, respectively, are presented due to the exceed $(NH_4)_2HPO_4$ decomposed.[39] Besides, there is a broad endothermic peak at 600~700°C due to the phosphate exhibits a complex phase transition.[40] It can be seen that there no obviously weightlessness peak takes place after the temperature increasing up to 550°C suggesting that the active components on the surface of the γ-Al_2O_3 get stable after calcination 550°C.[49,41]

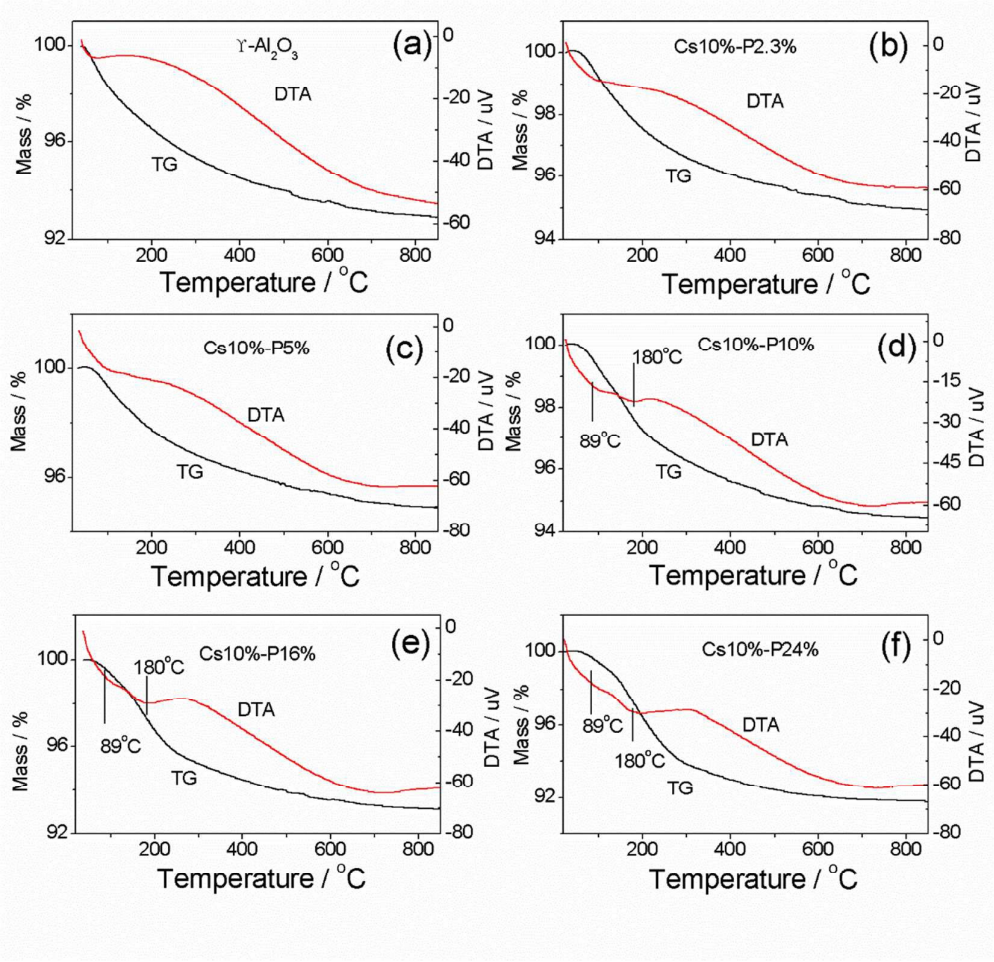

Figure 3. TG/DTA curves of Cs-P/γ-Al_2O_3 catalysts with different P-loadings before calcination: (a) γ-Al_2O_3, (b) 2.3%, (c) 5%, (d) 10%, (e) 16%, (f) 24%.

The XPS measurement of Cs-P/γ-Al_2O_3 catalyst is investigated to determine the chemical state of surface species. The P2p spectra are presented in Figure 4. We can see that the P2p spectra of all the samples have a relatively wide peak from 130.5 to 136.5 eV which indicated that the multi phosphate phases on the surface of the γ-Al_2O_3 support. The binding energies of the P 2p spectra for P_2O_5, PO_3^{-1}, $P_2O_7^{-4}$, PO_4^{-3} are 135.6, 134.5, 133.4, and 132.3 eV respectively.[42, 43] By means of XPS peak differentiation imitating analysis, as shown in Table 2, it can be seen that the catalyst is mainly composed by metaphosphate, pyrophosphate. With an increase of the P-loading, the P_2O_5 phase appears due to the excess amount of the $(NH_4)_2HPO_4$ decomposed. Besides, the proportion of phosphate changes indistinctively possibly due to the interaction between the phosphor and γ-Al_2O_3 support to form a stable $AlPO_4$ phase. The XPS spectra of Cs 3d is presented in Figure 5f, the binding energies at 725.2 and 739.1 eV are of Cs 3d5/2 and Cs 3d3/2 spectra, respectively.[44] The FT-IR spectra of these catalysts also provides visible information about the interaction of active components Cs and P with alumina support as shown in Figure 5. A broad and smooth absorption band range from 500 - 900 cm^{-1} is the characteristic infrared spectrum of amorphous alumina which can be attributed to the disordered distribution of vacancies and the continuous distribution of bond length in an amorphous material.[45] There are three characteristic frequencies, namely, 1095, 1382 and 1519 cm^{-1} belonging to the symmetric bending, asymmetric bending and stretching vibration of Al-OH groups respectively.[46] The peaks at 1637 and 3455 cm^{-1} belong to the O-H stretching vibration. These spectra still present well resolved when Cs soaks on the alumina support. However, when P soaks on the alumina support, the three characteristic absorbing peaks disappear at higher P-loading for the interaction of active components Cs and P with alumina support. It can be seen that the Al-O-H (at 3463 cm^{-1}) species reduce slowly and the Al-O-P groups (at 1114 cm^{-1}) increase apparently with the increase of P-loading suggesting that cesium or phosphorus have a strong interaction with the Al-O-H to form Al-O-M.[47-50]

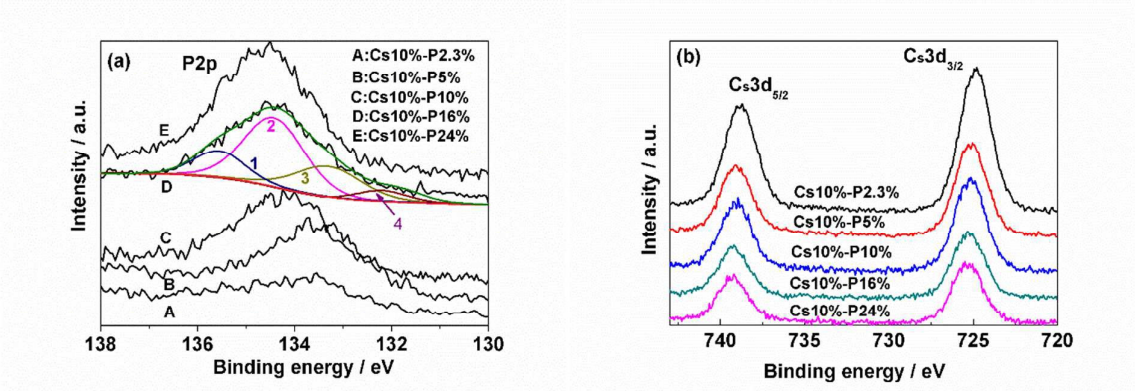

Figure 4. The P2p spectra (a) and Cs3d spectra (b)of the Cs-P oxides catalysts with different P-loadings; the fitted peaks 1, 2, 3, 4 are the P2p spectra of the P_2O_5, PO_3^{-1}, $P_2O_7^{-4}$, PO_4^{-3}, respectively.

Table 2. The percentage of total P atomic of the different phases.

	Molar percent (%)			
P-loading	P_2O_5	PO_3^{-1}	$P_2O_7^{-4}$	PO_4^{-3}
2.3%	0	61.0	28.3	10.7
5%	3.4	71.8	13.1	11.6
10%	6.9	68.3	13.3	11.6
16%	12.5	58.5	18.7	10.3
24%	47.0	32.2	10.1	10.7

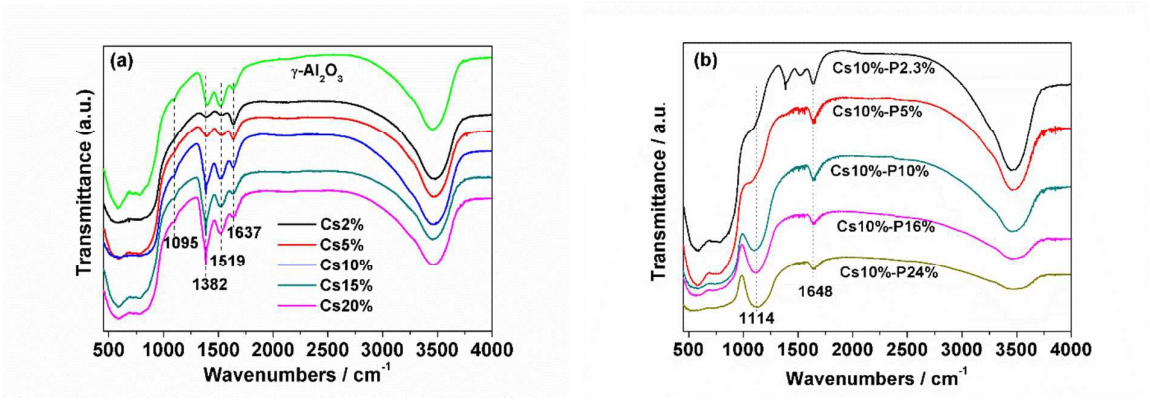

Figure 5. FT-IR spectra of the Cs-P/γ-Al_2O_3 catalyst with different P-loadings.

The morphology of Cs-P/γ-Al_2O_3 catalyst with different P-loadings is studied by TEM. As shown in Figure 6, the typical lamellar morphology, fibrous morphology, as well as spherical morphology which are the characteristic morphologies of γ-Al_2O_3 can be observed. The Cs-P/γ-Al_2O_3 catalysts morphologies change very little with the P-loading increasing and there also no bulk crystals are present also suggesting that the phosphorous species are well distributed on γ-Al_2O_3 surface.

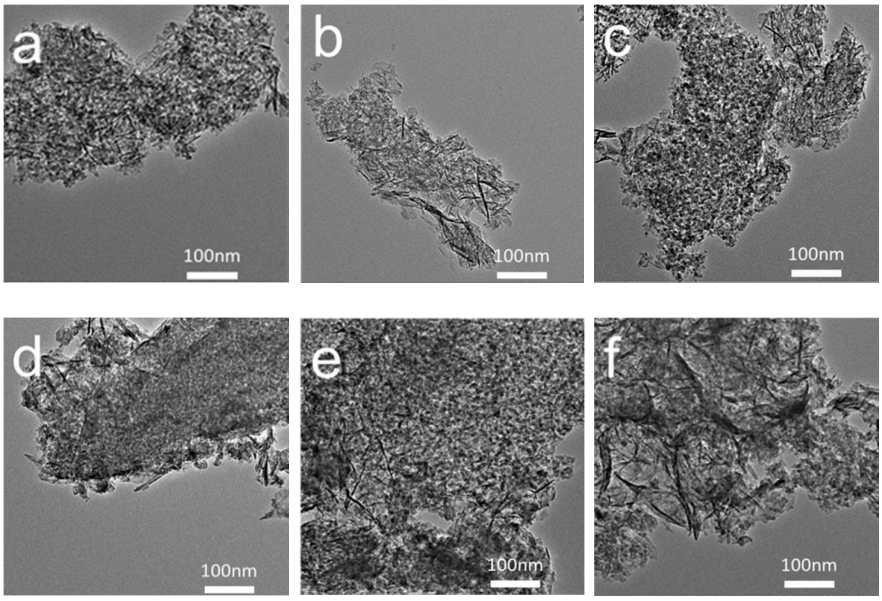

Figure 6. TEM images of the γ-Al_2O_3 (a) and Cs-P/γ-Al_2O_3 catalysts with different P-loadings: (b) 2.3%, (c) 5%, (d) 10%, (e) 16%, (f) 24%.

The surface area and pore size distribution of Cs-P/γ-Al_2O_3 catalysts are analyzed using N_2 adsorption–desorption. The results of the textural characterization of the Cs/γ-Al_2O_3 and Cs-P/γ-Al_2O_3 are shown in Table 3 and 4 respectively. From Table 3, it can be seen that the surface area decrease from 203.55 to 155.34 m^2g^{-1} and the pore diameter increase slowly from 8.28 to 8.63 nm with the Cs-loading increase. It is noted that the micropore volume increase slightly meanwhile the total pore volume decrease from 0.55 to 0.44 cm^3g^{-1}. These results indicate that Cs may be located mainly on the inner surface of the γ-Al_2O_3 mesopore structures. However, when P is introduced, with the P-loading increase, the specific surface area decreases rapidly from 176.41 to 62.99 m^2g^{-1} as well as the pore volume decreases from 0.45 to 0.23 cm^3g^{-1}, but the pore size quickly increased from 9.25 to 13.06 nm with P increase from 2.3 to 24%. These results likely to be attributed to the formation of the phosphate on γ-Al_2O_3 support, which blocked some γ-Al_2O_3 micropore.[51-52]

Table 3. The surface area, pore size and pore volume distribution of the Cs/γ-Al_2O_3 catalysts.

Amount of Cs (%)	2	5	10	15	20
S_{BET}(m^2/g)	203.55	192.56	178.01	166.96	155.34

Pore diameter (nm)	8.28	8.36	8.47	8.53	8.63
Pore volume(cm^3/g)	0.55	0.53	0.48	0.46	0.44

Table 4. The surface area, pore size and pore volume distribution profile of the Cs-P/γ-Al_2O_3 catalysts.

Amount of P (%)	2.3	5	10	16	24	γ-Al_2O_3
$S_{BET}(m^2/g)$	176.41	169.25	128.12	108.54	62.99	210.12
Pore diameter (nm)	9.25	10.36	11.02	12.16	13.06	8.51
Pore volume(cm^3/g)	0.45	0.43	0.35	0.27	0.23	0.52

3.2 Acid-base properties characterization

It reported that both acid and base site is important for the aldol condensation reaction. [10, 22, 23, 27] Such, the strength and quantitative analysis of base and acid sites on the surface of the catalysts are determined by stepwise temperature programmed desorption (TPD) of the CO_2 and NH_3. The desorption temperature reveals the base and acid strength of the catalysts. The higher desorption temperature, the stronger base or acid strength of the catalysts. From the CO_2 and NH_3-TPD profiles of the Cs/γ-Al_2O_3 with different Cs-loadings in Figure 7a and b, it can be seen that all the catalysts present two desorption peaks at rang of 100 ~ 300°C and 500 ~ 700°C corresponding to the weak and strong base or acid site respectively. From the desorption profiles of CO_2 (Figure 7a), the amount of weak and strong base site increased with Cs-loading increase, especially the change of strong base sites at high Cs-loading, suggesting that the addition of cesium carbonate generates new base sites. [22] As is well known, the surface acidity of aluminum oxides is due mainly to Lewis sites, incompletely coordinated aluminum ions on the surface. From the NH_3-TPD profile of γ-Al_2O_3 support as shown in Figure 7b, the NH_3 desorption takes place with three maxima desorption at 160, 330, 516~630 °C respectively suggesting at least 3 type Lewis sites on the surface.[53] The increased content of weak acid sits (at low temperature) can be ascribed to the Lewis acidity of Cs^+.[27] Therefore, with increasing Cs content, the content of weak acid sites continues to increase. At low Cs content, the content of strong acid site on the surface of Cs/γ-Al_2O_3 catalyst (at high temperature) decreases quickly as the result of the reaction of cesium with protons of the hydroxyls of alumina surface which is Brϕnsted acid site to form a surface species being a precursor of alkali metal aluminate.[54] However, at high Cs content, it increases significantly possibly due to the formation of CsO_2 phase which interact with NH_3 via one of its hydrogen atoms to a surface oxygen atom; and then a rapid proton exchange occurs among the surface species and generates a new acid site as temperature increases.[55] From the XRD patterns of the Cs/γ-Al_2O_3 catalysts, the diffraction intensity of cesium superoxide (CsO_2) phase significantly increases with Cs-loading increases from 10 to 20%. And from the FT-IR spectra of Cs/γ-Al_2O_3 catalyst, the peaks 1382 and 1519 cm^{-1} belonging to asymmetric bending and stretching vibration of Al-O-H groups respectively get stronger with Cs content increases. These results are consistent with the changes of strong acid site content.

It is reported that strong base and acid sits on the surface of the catalyst which does not correspond to high condensation but may aggravate carbonaceous deposits on the surface of the catalyst.[5, 23, 27] However, P is introduced to Cs-P/γ-Al_2O_3 catalysts, from the Figure 8, it can be seen that both CO_2 and NH_3 desorption peak at high temperature get reduced quickly, however, change little at low temperature. Therefore, addition of phosphorus can reduce the strong base and acid sites meanwhile maintaining the weak base and acid sites possibly due to the interaction between P and Cs to form the phosphate species. Amount the Cs-P/γ-Al_2O_3 catalysts, the Cs10%-P5%/γ-Al_2O_3 catalyst shows the highest amount of weak base and acid sites.

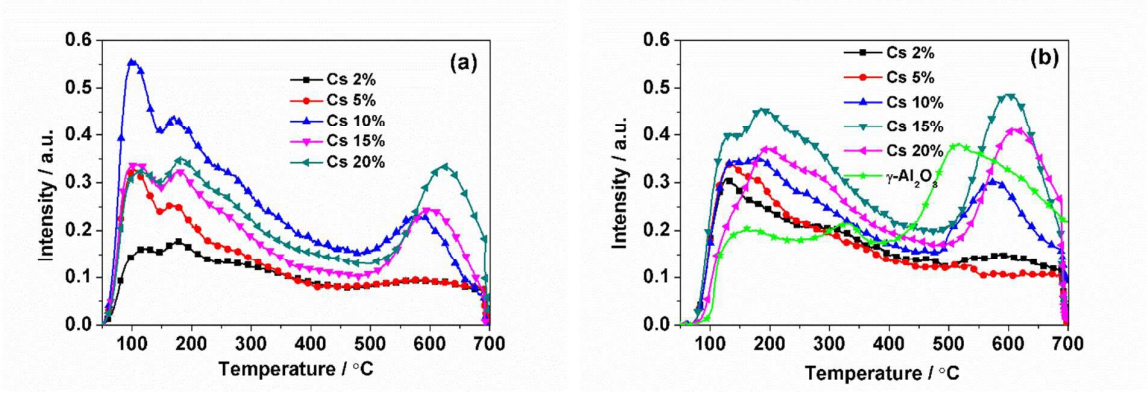

Figure 7. CO_2-TPD (a) and NH_3-TPD (b) profiles of the Cs/γ-Al_2O_3 with different Cs-loadings.

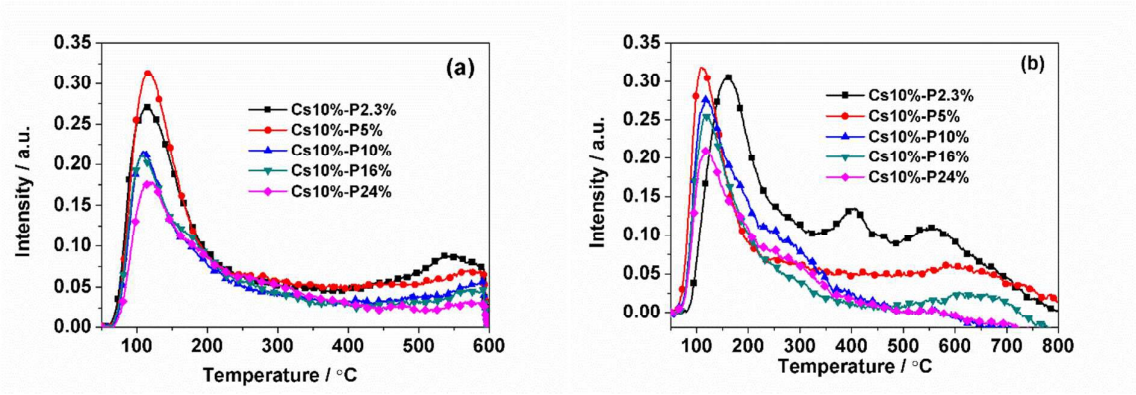

Figure 8. CO_2-TPD (a) and NH_3-TPD (b) profiles of Cs-P/γ-Al_2O_3 catalysts with different P-loadings.

3.3 Catalyst Performance

The catalytic performances of all the catalysts are evaluated using a continuous-flow fixed-bed tubular microreactor filled with 5 g catalysts. From the Figure 9, the activity of the Cs /γ-Al_2O_3 catalyst increase as Cs-loading increases from 2 to 10%, and then decrease quickly at higher Cs-loading due to large amount of strong base and acid sites which aggravate carbonaceous deposits on the surface of the catalyst. Besides, from the XRD data, the formation of the superoxide CsO_2 phase at higher Cs-loading which has no activity also consumes some active sites on the catalyst surface. So the activity of the Cs /γ-Al_2O_3 becomes very low at higher Cs-loading. After introducing P, from the performances of the Cs-P/γ-Al_2O_3 as shown in Figure 10, it can be seen that the yield of MA is obviously higher than that of Cs /γ-Al_2O_3 catalystsand the MA yield increases to 44.3% with P-loading up to 5% and then slowly decrease to 33.3% as P-loadings increase to 24%. The Cs10%-P5%/γ-Al_2O_3 show higher activity according to the yield and the selectivity due to it has higher weak base and acid density than other catalysts.

According to the literatures, the presence of the low-temperature peak correlates with catalytic activity and conversion of Ma.[8, 23] Based on the results and discuss above, in the aldol condensation reaction, the possible reaction route was shown in Figure 11. Firstly, Ma adsorbs on a base site to form α-C anion whereas formaldehyde adsorb on an acid site. And then the activated FA as an electrophile reacts with the α-C anion of Ma to form an intermediate aldol, which eventually condenses to MA and water.

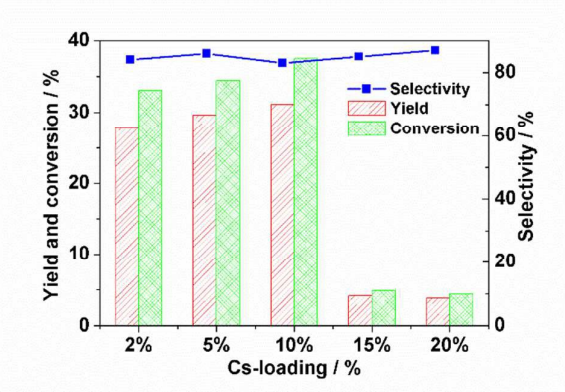

Figure 9. Catalytic performance of the Cs/γ-Al_2O_3 with different Cs-loading. Reaction was performed at 350°C, molar ratio of FA/Ma molar ratio is 1/5, liquid hourly space velocity is 1 h^{-1}.

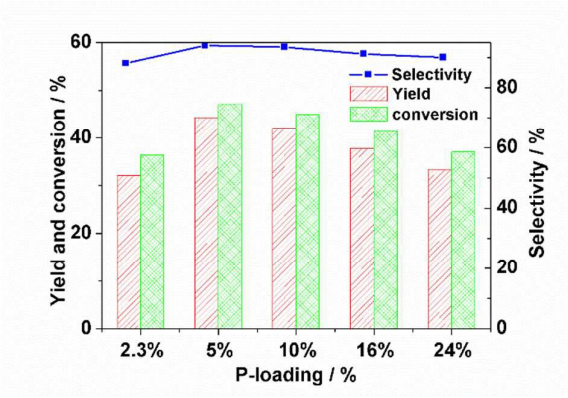

Figure10. The performances of the Cs-P/γ-Al_2O_3 with different P-loadings. Reaction condition: catalyst at 350°C. FA/Ma molar ratio is 1/5, liquid hourly space velocity was $1h^{-1}$, and FA is fed as trioxymethylene.

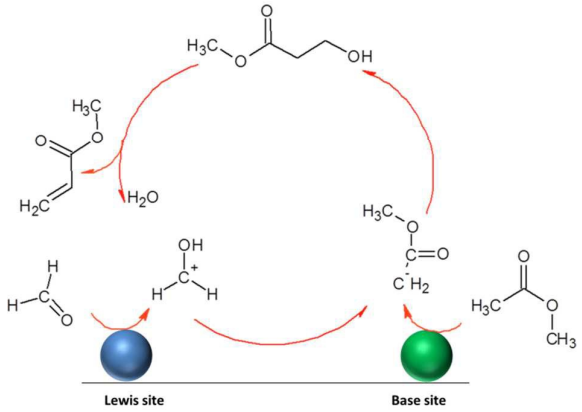

Figure 11. The vapour phase aldol condesation reaction route of Ma with FA over Cs-P/γ-Al_2O_3 catalyst.

3.4 RSM analysis and fitting the model

A Box–Behnken design (BBD) center-united design is adopted to design the process. The best-fitting models are determined by multiregression and backward elimination. The experimental and calculated results are shown in Table 5. The each value of MA yield is obtained with fixed reaction time of 2 h. As shown in Table 5, the MA yield increase from 26 to 45.4%, depending on the reaction conditions.

Table 5. The Box-Behnken design matrix of the variables in coded units and the experimental and predicted response value.

Run	Experimental variables in coded units			MA yield (%)	
	X_1	X_2	X_3	Experimental	predicted
1	3	340	30	29.9	29.9
2	3	360	45	28.6	28.4
3	3	380	30	30.5	31.5
4	3	360	15	26.0	25.4
5	5	360	30	41.6	41.6
6	5	380	15	32.9	32.6
7	5	360	30	41.6	41.6
8	5	340	45	35.0	35.3

9	5	340	15	28.9	29.7
10	5	360	30	41.6	41.6
11	5	380	45	42.9	42.1
12	5	360	30	41.6	41.6
13	5	360	30	41.6	41.6
14	7	340	30	38.6	37.6
15	7	380	30	45.4	45.5
16	7	360	15	31.5	31.7
17	7	360	45	43.3	43.9

Accordingly, through the RSM analysis, the second-order quadratic model relationship between the MA yield (Y) and the experimental variables in coded units is presented as Eq. 10

$$Y = 41.6 + 5.48X_1 + 2.41X_2 + 3.81X_3 + 1.55X_1X_2 + 2.3X_1X_3 + 0.97X_2X_3 - 4.04X_1^2 - 1.46X_2^2 - 5.21X_3^2 \quad (9)$$

where Y represents the MA yield and X_1, X_2, and X_3 are the coded variables (see Table 1) in aldol condensation reaction. It should be note that in Eq. 10 above, a positive sign (+) in front of a term exemplifies existence of a synergistic effect between the designated variables, whereas a negative sign (-) represents an antagonistic effect. [56] From the Eq. 10, MA yield has linear and quadratic effects by the three process variables. Molar ratio (X_1) has the strongest effect on the response since the coefficient of X_1 (β_1=5.48) is the largest and followed by reaction time X_3 (β_3=3.81) and temperature X_2 (β_2=2.41). The interaction effect between parameters X_1X_3 (β_{13}=2.3), is also stronger than the interaction effects between parameters X_1X_2 (β_{12}=1.55) and X_2X_3 (β_{23}=0.97). This may be due to cumulative effects of reaction parameters. [31] Figure 12 demonstrates a good linear correlation between the actual and predicted MA yield (calculated by Eq. 9).

The standard ANOVA is used to determine whether the quadratic model is adequate and fitted the data or not. Generally speaking, the p value is a tool to check whether a variable is significant or not. The smaller the P-value is, the more significant is the corresponding coefficient term. F-values are estimated by sum of squares, which are ratios of the effects of respective mean square and mean square error. [57,58] From Table 6, it can be seen that the second-order polynomial equation is highly reliable to represent the actual relationship between the response and the variables as the F and p value is 115.96 and less than 0.0001 respectively. The values of "Prob > F" are less than 0.05 indicating that model terms are significant. In this case, the coefficient of determination (R^2) is 0.9933 meaning that the polynomial model is accurate and possessed general applicability. The R^2-predicted of 0.8934 is in reasonable agreement with the R^2-adjusted of 0.9843. The high value of the adjusted determination coefficient (0.9848) demonstrates that the model is highly significant. The adequate precision of 33.4 is much greater than 4, indicating an adequate signal-to-noise ratio in this model discrimination. Apart from that, the lack-of-fit F value of 4.34 implies that the model is fitted to all data.

The response (MA yield) should be checked for the maximum and minimum ratios. If a ratio is higher than 10, the response transformation is required to improve the model.[38] In this case, the ratio is 1.65 meaning that the transformation is not required. After the above discussion, it can be seen that the selected model is enough for predicting the MA yield and can be used to study the interaction between response and process parameters.

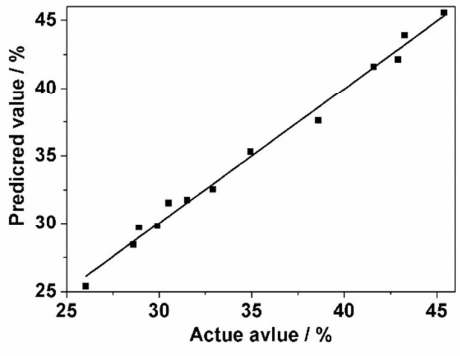

Figure 12. Experimental versus predicted values of the MA yield over the Cs10%-P5%/γ-Al_2O_3 catalyst.

Table 6. ANOVA for response surface quadratic model

Source	Sum of Squares	df	Mean Square	F-Value	p-value Prob > F
Model	646.66	9	71.85	115.96	< 0.0001
X_1	239.81	1	239.81	387.01	< 0.0001
X_2	46. 56	1	46.56	75.14	< 0.0001
X_3	116.28	1	116.28	187.66	< 0.0001
X_1X_2	9.61	1	9.61	15.51	0.0056
X_1X_3	21. 16	1	21.16	34.15	0.0006
X_2X_3	3.8	1	3.8	6.14	0.0424
X_1^2	68.64	1	68.64	110.77	< 0.0001
X_2^2	9.01	1	9.01	14.53	0.0066
X_3^2	114.4	1	114.4	1184.62	< 0.0001
Residual	4.34	7	0.62		
Lack of Fit	4.34	3	1.45		
Pure Error	0	4	0		
Cor Total	651	16			

R^2=0.9933; R^2(adjusted)=0.9848; R^2(predicted)=0.8934; Adeq Precision =33.417

On the basis of the predicted model, the interactions between variables have significant effects on the MA yield. Hence, the interactions of the parameters are invested by the response surfaces of the model plotted with a function of two variables by keeping other variables at a constant. Their corresponding three-dimensional response surface plots and two-dimensional interaction plots (contour) for the MA yield are shown in Figures 13. The effect of reaction time and molar ratio of Ma to FA on MA yield is shown in Figure 13a and a'. As the regression coefficients of the interaction terms (β_{13}=2.3) between parameters X_1X_3 is higher than another tow interaction terms X_1X_2 (β_{12}=1.55) and X_2X_3 (β_{23}=0.97), the MA yield is significantly influenced by the interaction between the molar ratio and reaction time. At low molar ratio, the MA yield increases with reaction time and then decreases passing a maximum at 30 min possibly due to the influence of the surface diffusion lead to carbon deposits from the decomposition of FA. However, the decreasing trend gets more and more inconspicuous at higher molar ratio. With shape of contour curve nearly ellipse mound and p-value (0.0006) of the interaction term, it seems that the molar ratio (X_1) has more significant effect on the MA yield than reaction time (X_3). Similar changes also can be observed with an increase of molar ratio at a constant of reaction time due to excess Ma inhibits the diffusion of the formaldehyde and makes it not easily absorbed on the surface of catalyst.

The effect of interaction between molar ratio (X_1) and temperature (X_2) is presented in Figure 13b and b'. The interaction between the molar ratio and temperature is also significantly influenced the MA yield, as the regression coefficients of the interaction terms between parameters X_1X_2 is 1.55. From the shape of contour curve (Figure 13b') and p-value (0.0056) of the interaction term, it can be seen that the molar ratio has stronger influence than the temperature which can be also prove from the regression coefficients of molar ratio (β_1=5.48) and temperature (β_3=2.41). Generally, at higher temperature, mass transfer rates among the reactants accelerate as the molecules gain more kinetic energy, and eventually lead to higher conversion in a shorter period.[59] Here, it can be also observed that the MA yield increases with the temperature from 340 to 380°C. However, at low temperature, the MA yield reduces slightly at higher the molar ratio and the possible explain is that the excess Ma inhibits the diffusion of the formaldehyde and makes it not easily absorbed on the surface of catalyst.

Figure 13c and c' shows the influence of the interaction between temperature (X_2) and reaction time (X_3) on the MA yield with a fairly low P-value 0.0424. Apparently, X_3 (β_3=3.81) has a stronger influence than X_2 (β_2=2.41). The yield of MA increases linearly up to a certain value with reaction time (X_2 = 30 min) at a given temperature and then decline possibly due to the external diffusion control to make the decomposition of the FA before reaction with Ma. On the other hand, a moderate increase of MA yield with X_3 is observed at a constant X_2 due to higher mass transfer rates at higher temperature.[49]

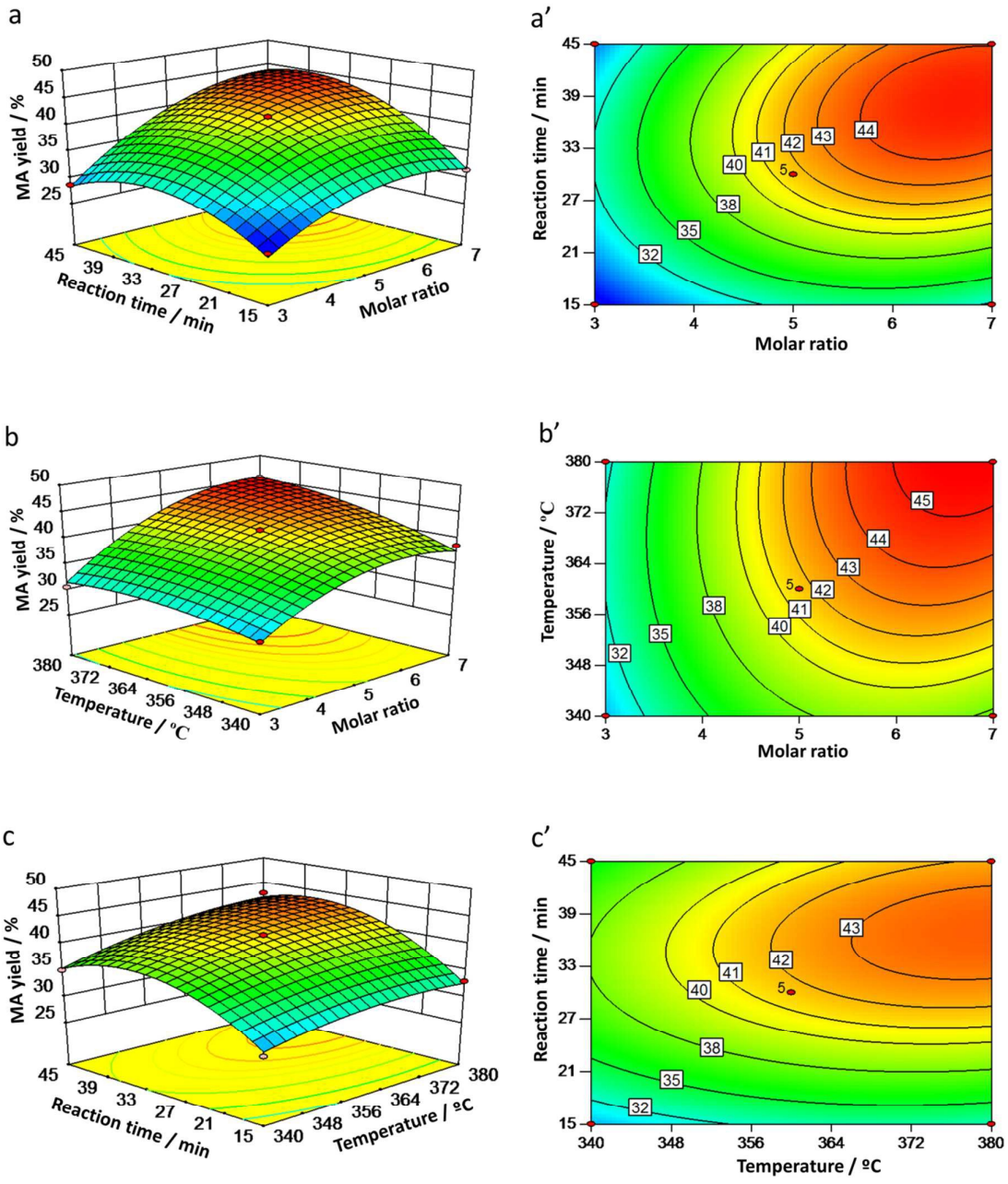

Figure 13. Three-dimensional response surface plots and two-dimensional interaction plots (contour) for the MA yield over Cs10%-P5%/γ-Al_2O_3 catalyst as a function of reaction time and molar ratio of Ma to formaldehyde (a and a'); temperature and molar ratio (b and b'); temperature and reaction time (c and c') respectively at constant c of 2 h on a fixed bed with 5 g catalyst.

In order to generate optimal conditions for the aldol condensation reaction to produce MA, numerical feature of the Design-Expert Version 8.0.6 software is applied. The independent parameters used in numerical optimization are including Ma/FA molar ratio (X_1), temperature (X_2), and reaction time (X_3). The MA yield is set to maximum value. Subsequently, 3 solutions for the optimum conditions are generated by the software. The optimal process conditions for the aldol condensation reaction over Cs10%-P5%/γ-Al_2O_3 catalyst are selected to be: X_1 = 6.83, X_2 = 380°C, and X_3 = 35.72 min. Under these conditions, the yield of MA reaches a maximum of 46.2%. For convenience, the optimum parameters are converted as follows: X_1 = 5, X_2 = 380°C, and X_3 = 35 min. In order to confirm the fit of the

predicted and actual data, three parallel experiments are performed under the condition above and showed an average yield of 47.1%, which is reasonably close to the predicted value and is regarded as satisfactory under the current constraints of the experiment.

3.5 Pseudohomogeneous Kinetic Model.

As discussed above kinetic model, the independent experiments are performed at different reaction temperature under a given optimum parameters. The Changes of FA concentration along with different reaction time at 613, 623, 633, and 643 K are shown in Figure 14 respectively. The curves of nonlinear fitting are drawn, and fit the data of experiments very well as all the R^2 is higher than 0.99.. And the plots of lnr vs lnC_{FA} are shown in Figure 15. Both reaction order a and lnk are obtained by linear regression. The four fit curves are approximately parallel straight lines and $R^2 > 0.99$ indicating that simplified kinetic equation is reasonable and suitable for the aldol condensation reaction in the reaction temperature 613-643K. The mean value of the reaction order a is 1.88.

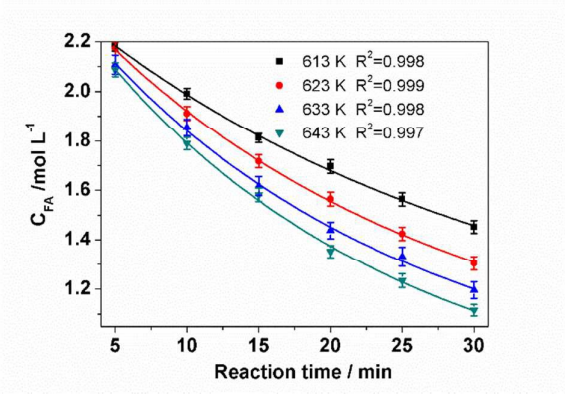

Figure 14. The changes the FA concentration along with the reaction time and the correspongding fit curve over 6 g Cs10%-P5%/γ-Al_2O_3 catalyst at different reaction temperatures, keeping the Ma/FA molar ratio of 5.

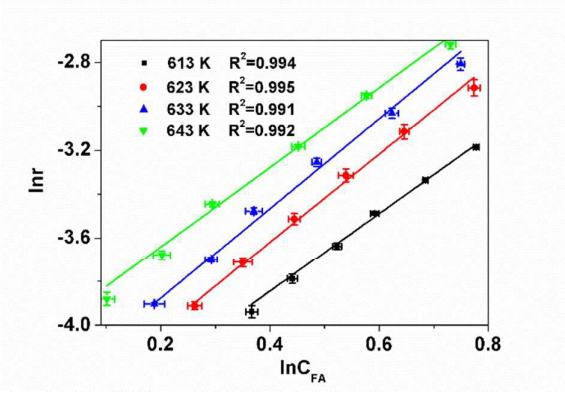

Figure 15. The plot of the lnr vs. lnC_{FA} to obtain the reaction order a and lnk.

The dependence of the reaction constants on reaction temperature is described by the Arrhenius equation (eqs.7 and 8). The value of reaction rate constants (k) is observed to be increased with reaction temperature increasing. The plot of lnk vs. 1/T is represented by a straight line (Figure 16). Both the frequency factor A and the activation energy Ea are obtained by linear regression. The pre-exponential frequency factor (A) and activation energy (Ea) for aldol condensation of the FA with Ma are calculated to be 1226.6 L min^{-1} mol^{-1} and 59.491 kJ mol^{-1}, respectively. The R^2 is 0.993 higher than 0.99 indicating the reasonable accurate.

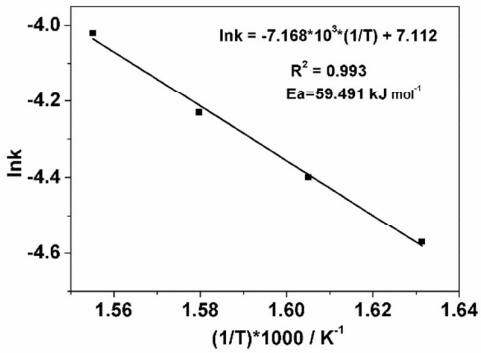

Figure 16. Arrhenius plot of FA with Ma over 6 g Cs10%-P5%/γ-Al_2O_3 catalyst at different reaction temperatures, keeping the Ma/FA molar ratio of 5 to obtain activation energy (Ea) and pre-exponential frequency factor (A)

3.6 Catalyst Stability and regeneration

The activity, strength and stability of the catalyst would bright future in commercial application. A good stability has been one of the key questions for the vapor-phase aldol condensation of Ma with FA. The cokes formed on active sites of the catalyst make the activity lose quickly and together with other technical problems block the catalyst from commercialization. The stability and regeneration of Cs-P oxides catalyst are also investigated and shown in Figure 17. It can be seen that the activity (base on the yield of MA) decrease about 50% after reaction 100 h as result of the formation of carbonaceous deposits. The used catalyst is characterized by TG/DTA with a heating rate of 5 °C min^{-1}. As shown in Figure 19a, the TG curve have a distinct weight loss from 300 to 450°C accompanied with a big exothermic DTA peak due to the coke combustion with O_2. Therefore, the deactivated catalyst can be regenerated by removing carbonaceous deposits at high temperature in a stream of air. The higher temperature, the faster carbonaceous deposits are removed. But high temperature processing for long time is not conducive to the catalyst. The used Cs-P/γ-Al_2O_3 catalyst is calcined at 380 and 400 °C respectively and is revealed by the TG and DTA curves in Figure 19b. It can be seen that there is an obvious mass loss between 700 and 800 °C after calcined at 380°C for 6h. However, it does not appear after calcined at 400°C for 6 h. The possible explanation is that the more stable carbonaceous deposits are formed after calcined at 380°C. Therefore, the used catalyst is calcined at 400 °C to remove carbonaceous deposits and the performances of the regenerated catalyst are shown in Figures 17b, c and d. It can be seen that the activity is relatively stable after total reaction time for 400 h.

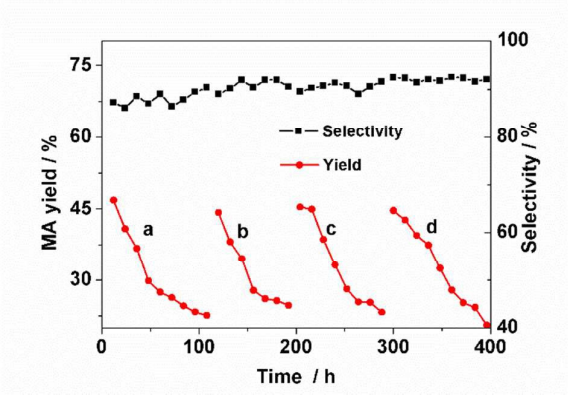

Figure 17. Stability of the Cs-P/γ-Al_2O_3 catalyst in the reaction of FA with Ma. Reaction condition: catalyst 5g. Ma/FA molar ratio is 5/1, and FA is fed as trioxymethylene.

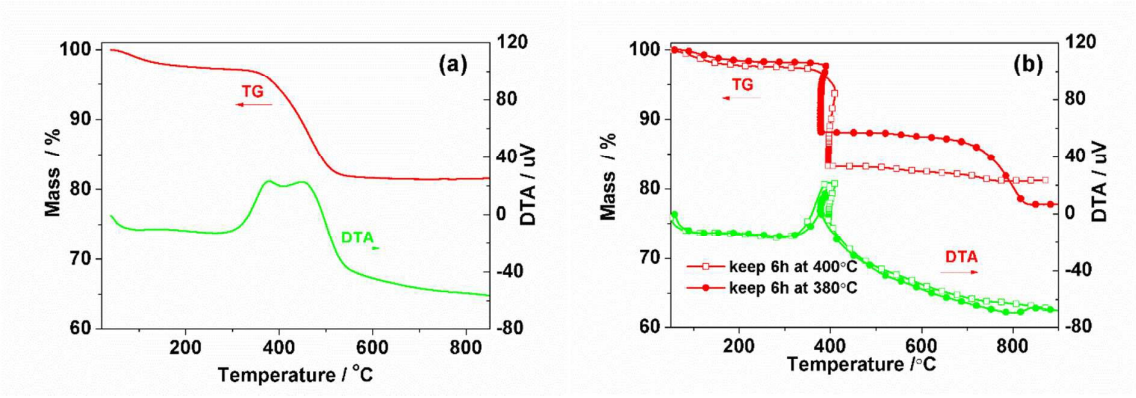

Figure 18. TG/DTA curves of the used Cs-P/γ-Al_2O_3 catalyst (a) with a heating rate of 5 °C min^{-1}, (b) keeping at 400 and 380°C for 6h.

4. Conclusions

The Cs/γ-Al_2O_3 and the Cs-P/γ-Al_2O_3 catalyst are prepared and studied. The Cs/γ-Al_2O_3 catalyst presents strong base and acid sites at higher loading which are not expected. However, the addition of P to Cs-P-/γ-Al_2O_3 catalyst can decrease the density of strong base and acid sites to improve the Cs-P/γ-Al_2O_3 catalyst activity. The Cs10%-P5%/γ-Al_2O_3 show higher activity according to the yield and the selectivity due to it has higher weak base and acid density than other catalysts. The process is optimized by RSM with three important variables including Ma/FA molar ratio, reaction time and reaction temperature and the analysis shows that molar ratio (X_1) has the strongest effect on the response since the coefficient of X_1 (β_1=5.46) is the largest and followed by reaction time X_3 (β_3=3.8) and temperature X_2 (β_2=2.42). And the data obtained from experiments is also interpreted using the PH kinetic model incorporating the effects of reaction temperature and the pre-exponential frequency factor (A) and activation energy (Ea) for aldol condensation of the FA with Ma are calculated to be1226.6 L min^{-1} mol^{-1} and 59.491 kJ mol^{-1}, respectively. The activity decreased slowly due to the carbon deposition on the surface of the catalyst which can be regenerated by calcined at 400°C under air atmosphere. After total reaction for 400 h, the activity of the Cs10%-P5%/γ-Al_2O_3 catalyst still keep the initial activity after regeneration.

Acknowledgements

This work was supported by the National Basic Research Program of China (2015CB251401), The National Natural Science Funds for Distinguished Young Scholar (No.21425625), and National Science Fund for Excellent Young Scholars (21422607), and Beijing Nova Programme (Z121111000250000).

References

1 K. Nagai, *Applied Catalysis A: General,* 2001, **221**, 367−377.

2 M. Ai, *Journal of Catalysis,* 1987,**107**, 201-208.

3 M. Ai, *Applied Catalysis A: General,* 1988, **36**, 221-227.

4 J. J. Spivey, M. R. Gogate, J. R. Zoeller and R. D. Colberg, *Ind. Eng. Chem. Res.,* 1997, **36**, 4600-4608.

5 M. R. Gogate, J. J. Spivey and J. R. Zoeller, *Catal. Today,* 1997, **36**, 243-254.

6 S. Impellizzeri, S. Simoncelli, C. Fasciani, M.L. Marin, G.L. Hallett-Tapley, G.K. Hodgson and J.C. Scaiano, *Catal. Sci. Technol.*, 2015, **5**, 169-175.

7 F. Cai, W. Zhu and Guo. Xiao, *Catal. Sci. Technol.*, 2006, DOI: 10.1039/c6cy00085a.

8 O. H. Bailey, R.A. Montag and J.S. Yoo, *Applied Catalysis A: General,* 1992, **88**, 163-177.

9 P. T. Wierzchowski and L.W. Zatorski, *Catalysis Letters,* 1991, **9**, 411-414.

10 J. S. Yoo, *Applied catalysis A: General,* 1993, **102**, 215-232.

11 M. Ai, *Applied Catalysis A: General,* 2005, **288**, 211-215.

12 M. Ai, *Catalysis Today,* 2006, **111**, 398-402.

13 R. Razzaq, C. Li, N. Amin, S. Zhang and K. Suzuki, *Energy Fuels* 2013, **27**, 6955−6961.

14 F. Jing, B. Katryniok, F. Dumeignil, E. Bordes-Richard and S. Paul, *Catal. Sci. Technol*., 2014, **4**, 2938-2945.

15 L. Jiang, Y. Diao, J. Han, R. Yan, X. Zhang and S. Zhang, *Chinese Journal of Chemical Engineering,* 2014, **22**, 1098-1104.

16 J. J. Creasey, A. Chieregato, J. C. Manayil, C. M. A. Parlett, K. Wilson and A. F. *Lee, Catal. Sci. Technol*., 2014, **4**. 861-867.

17 G. Parameswaram, M. Srinivas, B. Hari Babu, P. S. Sai Prasad and N. Lingaiah, *Catal. Sci. Technol*., 2013, **3**, 3242-3249

18 R. A. Otaibi, W. Weng, J. K. Bartley, N. F. Dummer, C. J. Kiely and G. J. Hutchings, C*hemcatcham,* 2010, **2**, 443-452.

19 M. Ai, *Applied Catalysis A: General,* 1990, **63**, 365-373.

20 M. Ai, *Applied catalysis A: General,* 2003, **252**, 185-191.

21 B. Li, R. Yan, L. Wang, Y. Diao, Z. Li and S. Zhang, *Catal. Lett.,* 2013, **143**, 829-838.

22 B. Li, R. Yan, L. Wang, Y. Diao, Z. Li and S. Zhang, *Ind. Eng. Chem. Res*., 2014, **53**, 1386-1394.

23 J. Tai, R. J. Davis, *Catalysis Today,* 2007, *123*, 42-49.

24 S. G. A. Ferraz, F. M. Z. Zotin, L. R. R. Araujo and J. L. Zotin, *Applied Catalysis A: General,* 2010, **384**, 51-57.

25 R. Razzaq, C. Li, M. Usman, K. Suzuki and S. Zhang, *Chemical Engineering Journal,* 2015, **262**, 1090-1098.

26 S. Sartipi, M. Makkee, F. Kapteijn and J. Gascon, *Catal. Sci. Technol*., 2014, **4**, 893-907.

27 J. Yan, C. Zhang, C. Ning, Y. Tang, Y. Zhang, L. Chen, S. Gao and Z. Wang, *J. Ind. Eng. Chem*., 2015, **25**, 344-351.

28 A. H. M. Fauzi, N. A. S. Amin, *Energ. Convers. Manage.,* 2013, **76**, 818-827.

29 I. Noshadi, N. A. S. Amin, R. S.Parnas, *Fuel*, 2012, **94**, 156-164.

30 L. Wai, X. Li, L. Yanxun, L. Tingliang, L. Guoji, *Chem. Eng. Technol.,* 2013, **36**, 559-556.

31 P. Yin, W. Chen, W. Liu, H. Chen, R. Qu, X. Liu, Q. Tang, Q. Xu, *Bioresour. Technol*. 2013, **140**, 146-151.

32 P. Berteau, M.A. Kellens and B. Delmon, *J. Chem. Soc. Faraday Trans*., 1991, **87**, 1425-1431.

33 G. Busca, G. Ramis, V. Lorenzelli, P.F. Rossi, A. La Ginestra and P. Patrono, *Langmuir,* 1989, **4**, 911-916.

34 J. M. Lewis and R. A. Kydd, *J. Catal*., 1991, **132**, 465-471.

35 G. Ramis, P.F. Rossi, G. Busca, V. Lorenzelli, A. La Ginestra and P. Patrono, *Langmuir,* 1989, **4**, 917-923.

36 F. Abbattista, A. Delastro, G. Gozzelino, D. Mazza, M. Vallino, G. Busca and V. Lorenzelli, *J. Chem. Soc. Faraday Trans*., 1990, **86**, 3653-3659.

37 K. Gishti, A. Iannibello, S. Marengo, G. Morelli and P. Tittarelli, *Appl. Catal*., 1984, **12**, 381-390.

38 Stat-Ease. Multifactor RSM tutorial (part 2-optimization). Design-expert software version 7.1.5, user's guide; 2008.

39 C. Muntean, W. Brandl, A. Iovi and P. Negrea, *Thermochimica Acta.*, 2005, **439**, 21-26.

40 G. Zhang, Z. Peng and C. Li, 2015, DOI 10.1007/s10973-015-5192-x.

41 L. R. R. Araujoa, C. F. Scofield, N. M. R. Pasturaa and W. A. Gonzalez, *Materials Research,* 2006, **9**, 181-184.

42 R. Gresch, W. Muller-warmuth, *Journal of Non-Crystalline Solids*, 1979, **34**, 127-136.

43 W. E. Morgan, J. R. Van Wazer, and W.J. Stec, *J. Am. Chem. Soc.*, 1973, **95**, 751–755.

44 E. A. Podgornov, I. P. Prosvirin and V. I. Bukhtiyarov, *Catal. A: Chem*., 2000, **158**, 337–343.

45 Barker, Jr., A.S., *Physical Review*, 1963, **132**, 1474-1481.

46 A. Boumaza, L. Favaro, J. Lédion, G. Sattonnay, J. B. Brubach, P. Berthet, A. M. Huntz, P. Royc , R.Té tot, *Journal of Solid State Chemistry*, 2009, **182**, 1171–1176.

47 F. Yaripour, F. Baghaei, I. Schmidt and J. Perregaard, *Catalysis Communications,* 2005, **6**, 542–549.

48 K. S. Lee, *J. Phy. Chem. Solids,* 1996, **57**, 334-342.

49 S. Chen, Y. Zhang, M. Wu, W. Fang and Y. Yang, *Applied Catalysis A: General,* 2012, **431**, 151– 156.

50 J. Otomo, N. Minagawa, C. Wen, K. Eguchi and H. Takahashi, *Solid State Ionics,* 2003, **156**, 357–369.

51 C. Li, D. Hirabayashi and K. Suzuki, *Materials Research Bulletin,* 2011, **46**, 1307–1310.

52 M. Ai, *Applied Catalysis A: General,* 2003, **252**, 185–191.

53 N. M. Popova, React. *Kinet. Catal. Lett*. 1998, **65**,363-370.

54 J. Haber, *Applied Catalysis B: Environmental*, 2008, **77**, 278–283.

55 E. B. Burgina, E. N. Yurchenko, E. A. Paukshtis: *J. Mol. Struct.*, 1986, **147**, 193-201.

56 W. Yan, K. Chen, X. Zhang, Y. Kuang, X. Tang and X. Han, *Journal of Industrial and Engineering Chemistry,* 2015, **29**, 185–193.

57 K. T. Tan, K. T. Lee and A. R. Mohamed, *Bioresour. Technol*., 2010, **101**, 965-969.

58 C. Chang, G. Xu and X. Jiang, *Bioresour. Technol.,* 2012, **121**, 93-99.

59 A. H. M. Fauzi , N. A. S. Amin, *Energy Conversion and Management*, 2013, **76**, 818–827.